

Numerical model for tomographic image formation in transmission x-ray microscopy

Michael Bertilson,^{1,2} Olov von Hofsten,^{1,2} Hans M. Hertz,¹ and Ulrich Vogt^{1,*}

¹Biomedical and X-Ray Physics, Dept. of Applied Physics, KTH Royal Inst. of Technology/Albanova, 10691 Stockholm, Sweden

²Shared first authorship

*ulrich.vogt@biox.kth.se

Abstract: We present a numerical image-formation model for investigating the influence of partial coherence, sample thickness and depth-of-focus on the accuracy of tomographic reconstructions in transmission x-ray microscopes. The model combines wave propagation through the object by finite difference techniques with Fourier methods. We include a ray-tracing model to analyse the origin of detrimental stray light in zone plate-based x-ray microscopes. These models allow optimization of x-ray microscopy systems for quantitative tomographic imaging of thick objects. Results show that both the depth-of-focus and the reconstructed local absorption coefficient are highly dependent on the degree of coherence of the optical system.

©2011 Optical Society of America

OCIS codes: (340.0340) X-ray optics; (340.7460) X-ray microscopy; (110.4980) Partial coherence; (110.6955) Tomographic imaging.

References and links

1. A. Sakdinawat and D. Attwood, "Nanoscale X-ray imaging," *Nat. Photonics* **4**(12), 840–848 (2010).
2. W. Chao, B. D. Harteneck, J. A. Liddle, E. H. Anderson, and D. T. Attwood, "Soft X-ray microscopy at a spatial resolution better than 15 nm," *Nature* **435**(7046), 1210–1213 (2005).
3. D. Weiss, G. Schneider, B. Niemann, P. Guttman, D. Rudolph, and G. Schmahl, "Computed tomography of cryogenic biological specimens based on X-ray microscopic images," *Ultramicroscopy* **84**(3-4), 185–197 (2000).
4. H. N. Chapman and K. A. Nugent, "Coherent lens-less X-ray imaging," *Nat. Photonics* **4**(12), 833–839 (2010).
5. National Center for X-Ray Tomography, <http://ncxt.lbl.gov/>; BESSY II X-ray Microscope, http://www.bessy.de/bit/bit_station_list.php
6. P. A. C. Takman, H. Stollberg, G. A. Johansson, A. Holmberg, M. Lindblom, and H. M. Hertz, "High-resolution compact X-ray microscopy," *J. Microsc.* **226**(2), 175–181 (2007).
7. M. Uchida, G. McDermott, M. Wetzler, M. A. Le Gros, M. Myllys, C. Knoechel, A. E. Barron, and C. A. Larabell, "Soft X-ray tomography of phenotypic switching and the cellular response to antifungal peptoids in *Candida albicans*," *Proc. Natl. Acad. Sci. U.S.A.* **106**(46), 19375–19380 (2009).
8. G. Schneider, P. Guttman, S. Heim, S. Rehbein, F. Mueller, K. Nagashima, J. B. Heymann, W. G. Müller, and J. G. McNally, "Three-dimensional cellular ultrastructure resolved by X-ray microscopy," *Nat. Methods* **7**(12), 985–987 (2010).
9. B. R. Frieden, "Optical transfer of the three-dimensional object," *J. Opt. Soc. Am.* **57**(1), 56–66 (1967).
10. N. Streibl, "Three-dimensional imaging by a microscope," *J. Opt. Soc. Am.* **2**(2), 121–127 (1985).
11. Y. Wang, C. Jacobsen, J. Maser, and A. Osanna, "Soft X-ray microscopy with a cryo scanning transmission X-ray microscope: II. Tomography," *J. Microsc.* **197**(1), 80–93 (2000).
12. O. von Hofsten, P. A. C. Takman, and U. Vogt, "Simulation of partially coherent image formation in a compact soft X-ray microscope," *Ultramicroscopy* **107**(8), 604–609 (2007).
13. M. Nevière and E. Popov, *Light Propagation in Periodic Media*, (Marcel Dekker, 2003).
14. J. Zhenle, F. Junmei, and F. Enxin, "A simple wide-angle beam-propagation method for integrated optics," *Microw. Opt. Technol. Lett.* **14**(6), 345–347 (1997).
15. A. N. Kurokhtin and A. V. Popov, "Simulation of high-resolution x-ray zone plates," *J. Opt. Soc. Am. A* **19**(2), 315–324 (2002).
16. G. R. Hadley, "Transparent boundary condition for beam propagation," *Opt. Lett.* **16**(9), 624–626 (1991).
17. B. L. Henke, E. M. Gullikson, and J. C. Davis, "X-ray interactions: Photoabsorption, scattering, transmission, and reflection at E = 50–30,000 eV, Z = 1–92," *At. Data Nucl. Data Tables* **54**(2), 181–342 (1993).
18. C. Messaoudi, T. Boudier, C. Sorzano, and S. Marco, "TomoJ: tomography software for three-dimensional reconstruction in transmission electron microscopy," *BMC Bioinf.* **8**(1), 288 (2007).
19. <https://www.sonoma.edu/users/c/cannon/biomineralTEM.html>

1. Introduction

X-ray microscopy is an established technique for nanoscale imaging with applications in cell biology, as well as material and environmental science [1]. By using soft x-rays in the water-window ($\lambda = 2.3 - 4.4$ nm; $E = 284 - 540$ eV) a natural contrast between carbon and water is provided for cell imaging, and zone-plate optics typically provide a resolution of 15 - 30 nm [2]. The technique allows whole cells (5-10 μm in diameter) to be imaged at high resolution in their near-native environment without staining or slicing [3], an advantage only met by coherent diffraction imaging [4]. X-ray microscopes are installed at a number of synchrotron radiation sources around the world [5], and laboratory instruments are also in use [6]. Determination of three-dimensional structure is possible by computed tomography, which has been shown to provide 50-70 nm isotropic resolution [7,8]. In addition, the method allows for classification of different intra-cellular structures according to their local absorption coefficient (LAC) via Beer-Lambert's law, in analogy to the macroscopic x-ray imaging of computed tomography. However, x-ray microscopes produce images of the object, instead of geometrical projections. Therefore, the accuracy of the reconstructed LAC depends on the coherence-dependent contrast transfer of the optic, artifacts from the reconstruction, sample thickness as well as stray light.

Analytical methods for calculating the image formation of a three-dimensional object in microscopes have been presented for both incoherent [9] and partially coherent systems [10]. These methods are limited to weakly scattering objects in the first Born approximation. The incoherent case has been applied numerically to the case of a scanning x-ray microscope [11] but the partially coherent case of transmission x-ray microscopy has so far not been investigated. Here we present a numerical model for partially coherent image formation of thick samples based on wave propagation through the object. It therefore also includes effects of multiple scattering. We apply the model to tomographic imaging in transmission x-ray microscopy and analyze the influence of partial coherence and optical transfer on the LAC and on depth-of-focus (DOF). The model allows quantitative analysis of 3D tomogram accuracy and system performance optimization. We also present results of ray-tracing simulations to determine stray light, produced by non-imaging orders of the zone plate, and evaluate ways to mitigate it. Stray light leads to errors in the LAC and cannot be subtracted from the image.

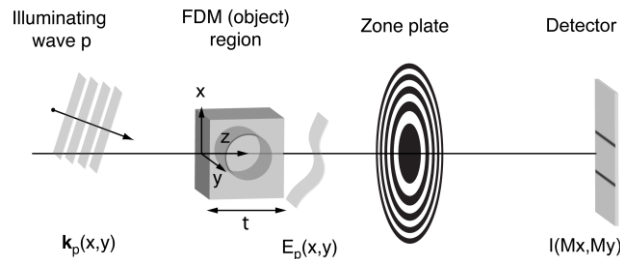


Fig. 1. Schematic of a transmission x-ray microscope setup with relevant coordinates. The illuminating waves originate from the condenser point p and propagate through the object. The resulting field behind the object is then imaged by the zone plate onto the detector.

2. Wave-propagation model

All existing transmission x-ray microscopes use critical illumination of the object by a condenser, which can be based on reflection or diffraction. The illuminated object is then imaged by the zone plate objective, which produces an image on a detector. The zone plate has a resolution close to its outermost zone width and by using a hollow-cone illumination, the strong 0th order is separated from the image. A schematic of an x-ray microscope is shown in Fig. 1, where the relevant coordinates of the optical system are also shown.

The imaging model is based on a previously published model limited to thin objects [12]. It approximates the zone plate as a thin lens and the condenser as a secondary incoherent source where each condenser point p contributes with a coherent image of the electric field $E_p(x, y)$ behind the object. This applies to most x-ray microscopes using synchrotron or laboratory sources. The final 2D image $I(Mx, My)$ is formed by the integration of these individually coherent but mutually incoherent images over the spectrum and is given by

$$I(Mx, My) = \sum_{\lambda} \sum_p S_{\lambda} \cdot \left| \mathcal{F}^{-1} \left(A_{\lambda}(\nu_x, \nu_y) \cdot \mathcal{F} \left(E_p(x, y) \right) \right) \right|^2, \quad (1)$$

where S_{λ} is the spectrum, M the magnification and \mathcal{F} the Fourier transform. The aperture function, given in spatial frequency coordinates (ν_x, ν_y) , includes chromatic aberrations by a wavelength-dependent defocus, Δf_{λ} , and is defined as

$$A_{\lambda}(\nu_x, \nu_y) = \begin{cases} \exp \left(ik \left(\nu_x^2 + \nu_y^2 \right) \frac{f \lambda^2 \Delta f_{\lambda}}{2(f + \Delta f_{\lambda})} \right) & \sqrt{\nu_x^2 + \nu_y^2} \leq \text{NA}_O / \lambda \\ 0 & \sqrt{\nu_x^2 + \nu_y^2} > \text{NA}_O / \lambda \end{cases}. \quad (2)$$

Here, $k = 2\pi/\lambda$ and $\Delta f_{\lambda} = \Delta f + f_{\lambda} - f$, where f_{λ} is the focal length of the zone plate at wavelength λ and Δf and f correspond to the defocus and focal length for the central wavelength, respectively. NA_O is the numerical aperture of the objective. Note that the aperture function can be changed arbitrarily, so other aberrations can easily be included in the model.

The fields $E_p(x, y)$ are obtained by propagating plane waves through the object using a finite difference method (FDM), which has been used previously in studies of x-ray optics [13]. Here we have used a wide-angle [14] Crank-Nicholson FDM scheme [15] with transparent boundary conditions [16]. To make the calculations computationally feasible, the FDM is carried out in the x - z plane, assuming a constant object cross section in the y -direction. The slowly varying component of the field just before the object, $u_j(z=0) = \exp(ik_x x_j)$, is propagated through the object in steps of Δz , where k_x is the x component of incident wave vector \mathbf{k}_p . Each step forms a linear equation system, $\mathbf{Z}_{\mp} \mathbf{u}(z + \Delta z) = \mathbf{Z}_{\pm} \mathbf{u}(z)$, manipulates the border elements to allow only out-going waves, and solves it. The matrices \mathbf{Z}_{\mp} are given by

$$\mathbf{Z}_{\mp} = \mathbf{I} \pm \frac{1}{4ik} \left(\Delta z \mp \frac{1}{ik} \right) \cdot \left(\frac{1}{(\Delta x)^2} \cdot \mathbf{A} + k^2 \mathbf{B} \right), \quad (3)$$

where \mathbf{I} is the identity matrix, Δx and Δz are the sampling grid spacings, and \mathbf{A} the second difference operator matrix. The non-zero elements of matrix \mathbf{B} are given by $B_{j,j} = n(x_i, z)^2 - 1$, where $n(x, z)$ is the local complex index of refraction of the object. The propagated wave $\mathbf{u}(z = t)$ is then expanded back to a 2D field, $E_p(x, y)$, taking the omitted phase gradient in the y -direction into account.

3. Imaging of thick samples

Figure 2 shows results of the wave-propagation model, clearly illustrating the deviations from geometrical projections due to the limited DOF. The calculations, performed in MATLAB, are based on a zone plate with a 30 nm outermost zone width and 100 μm diameter, a central wavelength of $\lambda = 2.48 \text{ nm}$ and a bandwidth of $\Delta\lambda/\lambda = 1/500$. The test phantom (Mylar features in water) is shown in Fig. 2(a), and has x-ray optical data taken from [17]. The illumination angles produce varying partial coherence, quantified by the coherence parameter m , defined as the ratio between the numerical aperture of the condenser and the numerical aperture of the objective. Figures 2(b) and 2(c) demonstrate the aperture matched ($m = 1$) and a more coherent case ($m = 0.3$) respectively. As a comparison, the completely coherent case ($m = 0$) is shown in Fig. 2(d). Both contrast and DOF increase with the coherence, especially for the larger features. This is partly explained by defocus phase contrast, that also causes artifacts in the image.

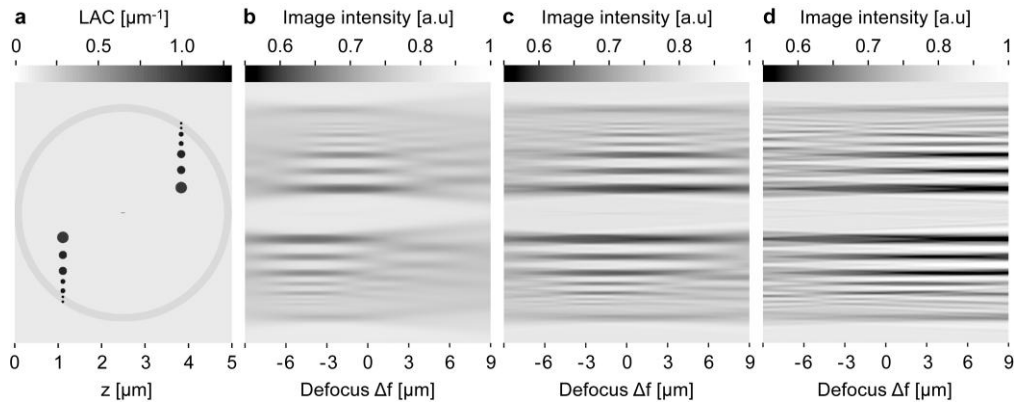


Fig. 2. Simulated focus series through a thick object using the wave-propagation model. (a) The phantom used in the simulations. (b) The aperture-matched condition, $m = 1$, yields the shortest DOF. (c) Partially coherent illumination, $m = 0.3$, provides a longer DOF and (d) a fully coherent illumination, $m = 0$, results in the longest DOF. Note the defocus phase contrast in (c) and (d) and the longer DOF for larger structures.

4. Tomographic imaging

The model allows us to analyze the accuracy of 3D reconstructions as well as optimizing future optical systems for x-ray microscopy. Figures 3(a)–3(c) shows simulated tomograms of a resolution test phantom using the same microscope parameters as in Fig. 2. The tomograms were reconstructed from projected densities of 360 calculated images, covering tilt angles of 0–180°, using a weighted back-projection algorithm [18] implemented in MATLAB. The accuracy of the reconstructed LAC decreases with feature size and sample radius. Furthermore, loss of resolution is larger in the angular direction compared to the radial. It is also clear that the aperture-matched case ($m = 1$) of Fig. 3(b) produces a higher resolution, but the more coherent case, Fig. 3(c), results in higher contrast and, thus, a higher LAC. In fact, while the incoherent case leads to an underestimation of the LAC, the partially coherent case leads to an overestimation due to the defocus phase contrast seen in Fig. 2(c). This shows that the coherence of the illumination plays an important role in x-ray tomography and needs to be taken into account when optimizing system parameters. The proper choice of these parameters (such as zone-plate optics, condenser and source) depends on the object (e.g., size, composition, structure) and imaging goals. Since the resulting 3D image quality critically depends on these parameters, full-system modeling is necessary for optimizing image quality and evaluating imaging performance. To further emphasize the influence of partial coherence on tomographic imaging, Figs. 3(d)–3(f) shows simulations using a realistic cell model [19].

All parameters and calculations are the same as the corresponding images of Figs. 3(a)–3(c). Again, the aperture-matched case yields a higher resolution, at the cost of a lower contrast.

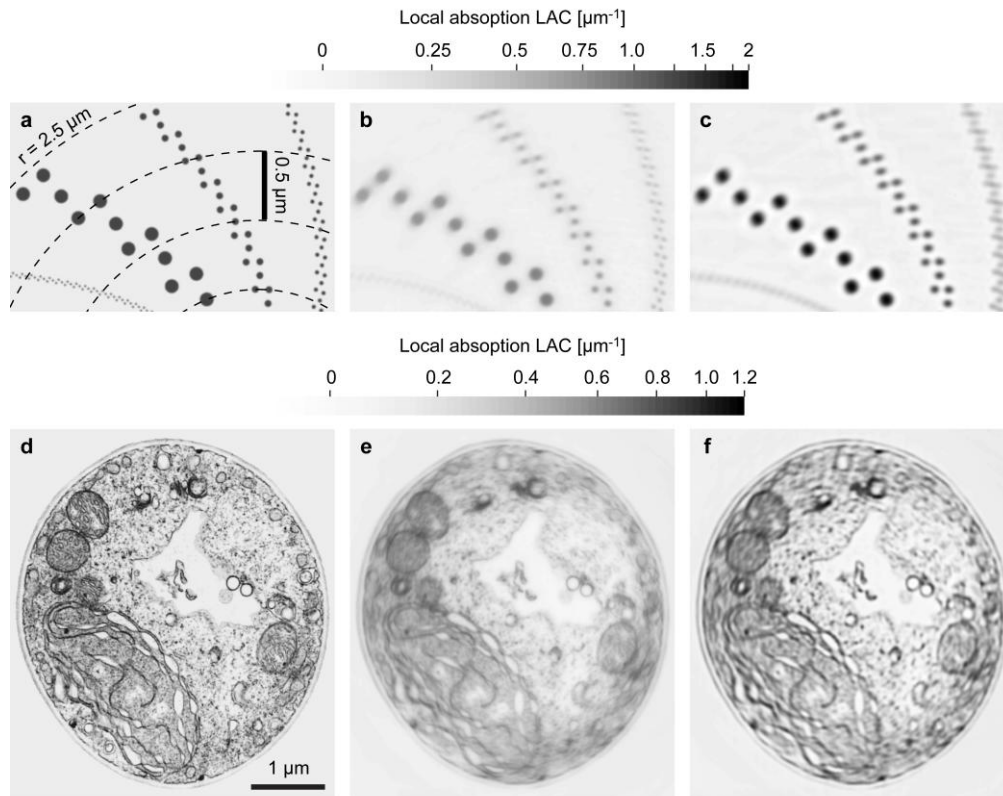


Fig. 3. Slices from reconstructed tomograms based on simulated images. (a) The resolution phantom contains Mylar features (15, 30, 50, and 100 nm in size and separated by two diameters) in water. The two cases of aperture-matched illumination (b) and partially coherent illumination (c) provide different contrast mechanisms and resolution. Note that the object is not shown in its whole. The grey levels correspond to the LAC and comparisons with the phantom indicate the error in the reconstructions. The realistic cell phantom (d) is simulated in (e-f) with the same coherence parameters as in (b-c), again showing the role of coherence in the illumination on tomographic reconstructions.

Thus the visual impression of Fig. 3(f) is preferred although the resolution is lower than in Fig. 3(e).

5. Stray light analysis

Ray-trace simulations of x-ray microscope systems complement the wave-propagation model by calculating stray light. The stray light is produced by other orders than the +1st order of the zone plate, with the -1st order being the main contributor. The ray-trace simulations were made in three dimensions by tracing a fan of 250 rays from each detector pixel, through the zone plate and back to the x-ray source. This procedure is equally accurate but computationally much faster than simulating from the source. The 1st and -1st diffraction order intensities were modeled, although the simulation can also include higher orders. The model includes aberrations of the condenser optic and simulations are made in the absence of an object. Just like the wave propagation model and the tomographic reconstructions, these calculations were performed using MATLAB.

Figure 4(a) shows the results of the ray-tracing model for the +1st order image intensity, I_1 , of the source and the -1st order stray-light intensity, I_s on the detector for the microscope

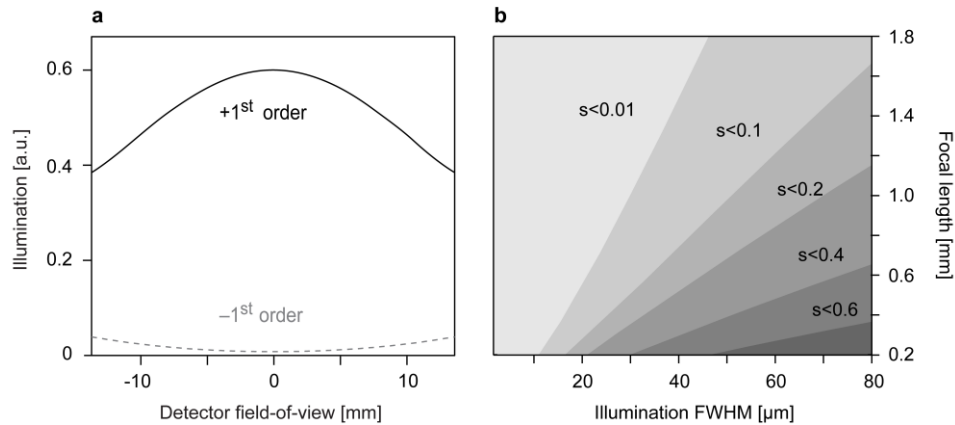


Fig. 4. Results of stray-light simulations under aperture-matched conditions. (a) Illumination light and stray light shown over the field-of-view for the 99 μm diam, 30 nm outermost zone width zone plate. (b) Stray-light ratio as a function of the source size in the object plane. The stray light increases for shorter focal lengths and for larger source sizes.

arrangement given earlier and a source size of 40 μm in the object plane. For this arrangement, the stray light is low in the center but increases off-axis. The stray light ratio, defined as I_s/I_1 , in the centre of the field of view is shown in Fig. 4(b) as a function of the object-plane source size and zone plate focal length. Clearly, the stray-light ratio increases with the source size and decreases with focal length. The stray light impairs contrast in the 2D microscope images, which results in an underestimation of the LAC in the 3D tomograms. The effect is stronger when studying highly absorbing specimens, since the resulting error in the LAC will be large. Furthermore, as x-ray microscopes push the resolution to below 10 nm, stray light will become more dominant as the focal lengths will be very small. This leads to longer exposure times and a higher deposited dose, potentially limiting the resolution by increasing noise. Note that systems using low-brightness large-size sources need to reduce stray light by apertures or source demagnification, potentially prohibiting tomographic image acquisition or increasing exposure times.

6. Conclusions

In summary, we have presented a numerical model for tomographic image formation of thick samples in transmission x-ray microscopes. The model was applied to study the influence of partial coherence on DOF and on the accuracy of tomographic reconstructions. We have also presented results from ray-trace simulations, which show that transmission x-ray microscopes may suffer from detrimental stray light. Both the degree of partial coherence and the stray light affects the accuracy of the reconstructed LAC, making it more challenging to categorize structures within cells. From the model we estimate that a resolution approaching 30 nm (half-period) over full 5- μm diameter objects should be achievable with a 30 nm outermost-zone-width zone plate. Higher resolution is obtained for smaller objects or smaller-diameter regions within larger objects. Such high-resolution quantitative 3D imaging of intact cells in their hydrated near-native state is of significant importance for studies of the function and structure of biological material on the nanoscale.

Acknowledgments

This work was supported by the Swedish Research Council, the Swedish Foundation for Strategic Research, and the Wallenberg Foundation.